Review Article | Thoracic Imaging

eISSN 2005-8330
https://doi.org/10.3348/kjr.2020.1136
Korean J Radiol 2021;22(4):634-651

Korean Journal of Radiology
KJR

Dynamic Chest X-Ray Using a Flat-Panel Detector System: Technique and Applications

Akinori Hata, MD, PhD[1], Yoshitake Yamada, MD, PhD[2], Rie Tanaka, PhD[3], Mizuki Nishino, MD, MPH[1], Tomoyuki Hida, MD, PhD[4], Takuya Hino, MD[1], Masako Ueyama, MD, PhD[5], Masahiro Yanagawa, MD, PhD[6], Takeshi Kamitani, MD, PhD[4], Atsuko Kurosaki, MD, PhD[7], Shigeru Sanada, PhD[8], Masahiro Jinzaki, MD, PhD[2], Kousei Ishigami, MD, PhD[4], Noriyuki Tomiyama, MD, PhD[6], Hiroshi Honda, MD, PhD[4], Shoji Kudoh, MD, PhD[9], Hiroto Hatabu, MD, PhD[1]

[1]Center for Pulmonary Functional Imaging, Department of Radiology, Brigham and Women's Hospital, Harvard Medical School, Boston, MA, USA; [2]Department of Diagnostic Radiology, Keio University School of Medicine, Tokyo, Japan; [3]Department of Radiological Technology, School of Health Sciences, College of Medical, Pharmaceutical and Health Sciences, Kanazawa University, Ishikawa, Japan; [4]Department of Clinical Radiology, Graduate School of Medical Sciences, Kyushu University, Fukuoka, Japan; Departments of [5]Health Care and [7]Diagnostic Radiology, Fukujuji Hospital, Japan Anti-Tuberculosis Association, Tokyo, Japan [6]Department of Diagnostic and Interventional Radiology, Osaka University Graduate School of Medicine, Osaka, Japan; [8]Clinical Engineering, Komatsu University, Ishikawa, Japan; [9]Japan Anti-Tuberculosis Association, Tokyo, Japan

Dynamic X-ray (DXR) is a functional imaging technique that uses sequential images obtained by a flat-panel detector (FPD). This article aims to describe the mechanism of DXR and the analysis methods used as well as review the clinical evidence for its use. DXR analyzes dynamic changes on the basis of X-ray translucency and can be used for analysis of diaphragmatic kinetics, ventilation, and lung perfusion. It offers many advantages such as a high temporal resolution and flexibility in body positioning. Many clinical studies have reported the feasibility of DXR and its characteristic findings in pulmonary diseases. DXR may serve as an alternative to pulmonary function tests in patients requiring contact inhibition, including patients with suspected or confirmed coronavirus disease 2019 or other infectious diseases. Thus, DXR has a great potential to play an important role in the clinical setting. Further investigations are needed to utilize DXR more effectively and to establish it as a valuable diagnostic tool.

Keywords: *Dynamic X-ray; Flat-panel detector; Functional imaging; Diaphragmatic motion; Ventilation; Perfusion*

INTRODUCTION

Evaluation of respiratory physiology and circulation is essential for management of patients with cardiopulmonary diseases (1, 2). In recent clinical practice, scintigraphy has been shown to play an essential role in these evaluations (3-5). CT and MRI are also utilized in lung functional imaging (6-11). In addition, attempts have been made to use X-ray-based techniques, including fluoroscopy and dynamic X-ray (DXR), for cardiopulmonary functional imaging (1, 2, 12).

Several studies have evaluated diaphragmatic motion using fluoroscopy and demonstrated its usefulness (13, 14). Furthermore, researchers have tried to visualize pulmonary ventilation and perfusion based on changes in X-ray translucency in digital fluoroscopic images using subtraction techniques (15-20). Theoretically, X-ray translucency changes depending on the volume of air and lung vessel/blood per unit volume in the image (Fig. 1). However, these techniques have not been widely used because of technical limitations, such as poor image quality and a small field of view (FOV).

DXR is a dynamic radiography technique that uses a flat-

Received: September 17, 2020 **Revised:** October 21, 2020
Accepted: October 26, 2020
The investigator, HH, is supported by R01CA203636 and U01CA209414 (NCI).
Corresponding author: Akinori Hata, MD, PhD, Center for Pulmonary Functional Imaging, Department of Radiology, Brigham and Women's Hospital, Harvard Medical School, 75 Francis Street, Boston, MA 02115, USA.
• E-mail: ahata1@bwh.harvard.edu

Korean Journal of Radiology
KJR

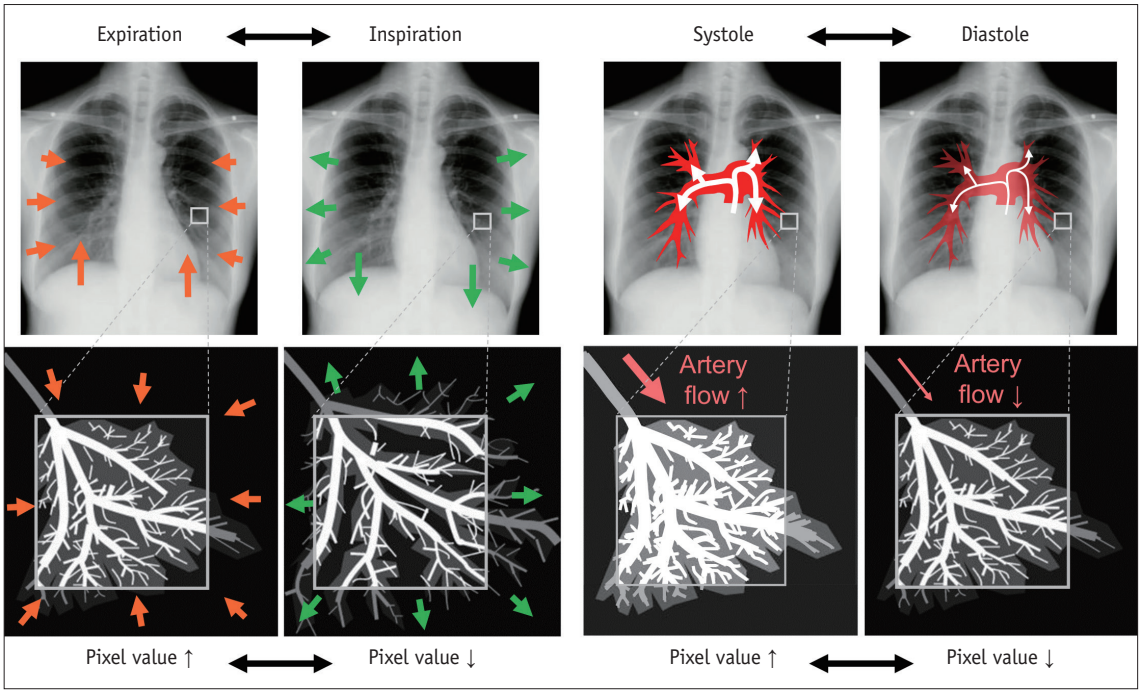

Fig. 1. The concept of changes in the pixel value (X-ray translucency) during the respiratory and cardiac cycles. The lung deflates during expiration, which results in a decrease in air and an increase in the lung vessel volume per unit volume. The pulmonary artery flow increases during the systole phase, which results in an increase in blood and vessel volume in the lung. During the inspiration and diastole phases, the opposite phenomena occur. The pixel value in the radiograph varies depending on the volume of air and the lung vessels per unit volume. This figure was made by us using materials used in reference 2.

panel detector (FPD) (1, 2). The FPD provides images with a large FOV that can entirely cover both lungs simultaneously during respiration. Recent improvements in the sensitivity of X-ray detectors have ensured sufficient image quality for analysis even at low radiation doses (21, 22). In addition, computer analysis and image processing can facilitate the interpretation of information obtained by DXR. These features of DXR have overcome the above-mentioned difficulties associated with fluoroscopy and enabled pulmonary functional image analysis.

DXR also shows advantages over other functional imaging modalities. First, scintigraphy, CT, and MRI are performed mainly in a supine position, while DXR can be performed in a standing or sitting position, reflecting physiologically relevant daily activity. Second, DXR provides sequential images with a high temporal resolution (7.5–30 frames per second [fps]) during respiration (23). Although area-detector CT can provide a relatively higher temporal resolution than scintigraphy, it cannot cover both lungs entirely in one scan, and the high temporal resolution in CT may not be practical because of the high radiation dose. Third, DXR is cost-effective, requires minimal space, and enables high throughput, which can reduce the associated medical costs (2).

Clinical reports of this DXR technique were published first by Tanaka et al. (24, 25). They experimentally evaluated diaphragm movement, pulmonary ventilation, and circulation in multiple normal participants and patients with pulmonary diseases as well as phantoms and animals (24-33). Their group also recently evaluated ventilation in 118 patients (34). Our group also assessed more than 100 healthy volunteers and more than 30 patients with chronic obstructive pulmonary disease (COPD) (23, 35-38). Our study elucidated the characteristics of diaphragmatic motion and demonstrated kinetic and physiological differences between normal individuals and COPD patients. Thus, evidence from DXR studies is now being accumulated. Here, we review the existing knowledge of DXR and introduce its clinical applications.

The DXR System: Equipment and Imaging Procedures

The DXR system uses sequential chest radiographs obtained by a dynamic FPD and a pulsed X-ray generator. Figure 2 shows an overview of the DXR system and its

https://doi.org/10.3348/kjr.2020.1136

clinical applications. This system uses indirect conversion to electronic FPDs, wherein X-ray energy is first converted to visible light in a scintillator layer, and the emitted light is then converted to electrical charges by an array of silicon-based photodiodes and subsequently read out by thin-film transistors (39). The pixel size, matrix, and overall image area of the flat panel were 388 x 388 microns, 1024 x 768, and 40 x 30 cm, respectively. The pulsed X-ray prevents excessive radiation exposure to the subjects by decreasing the duration of exposure. This system must have high homogeneity and uniformity in X-ray pulses (40).

Imaging is performed in a similar way as conventional chest radiography, except for the breathing pattern. The images are generally obtained in the standing/sitting position and the posteroanterior (PA) direction. Inspiratory and expiratory and/or breath-holding phases are included in the tidal or forced respiratory cycle, depending on the focus of the examination. Breath-holding phase images are used for cardiac phase analysis (27). The imaging rate should be greater than 7.5 fps for accurate evaluation of cardiac function and pulmonary circulation (41). For evaluation of respiratory function, it is necessary to include one whole respiratory cycle. A rate lower than 7.5 fps is acceptable for evaluation of respiration/ventilation considering the radiation dose, which can be adjusted by changing the imaging time, imaging rate, and source-to-image distance. The total patient dose can be less than the dose limit for two projections (PA and lateral views) of chest radiographs recommended by the International Atomic Energy Agency (1.9 mGy) (2, 42). One example of an imaging protocol is shown in Table 1 (1).

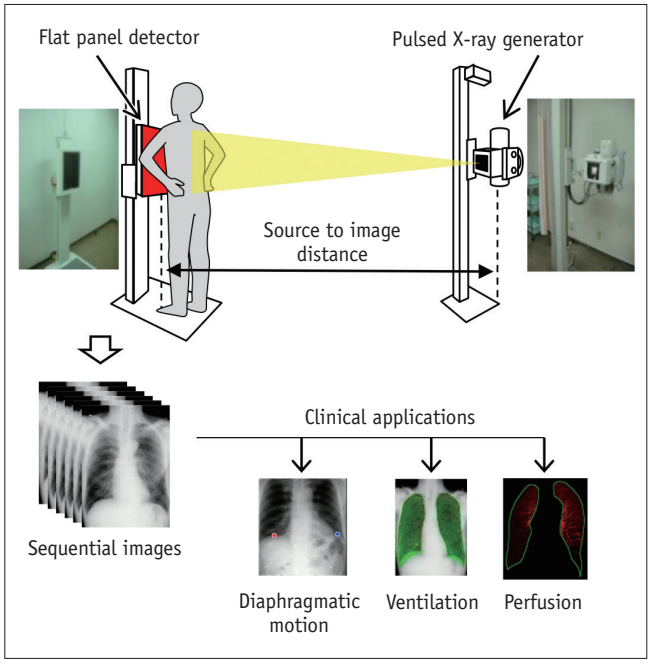

Fig. 2. Overview of the DXR system and its clinical applications.
The DXR system consists of a dynamic flat-panel detector and a pulsed X-ray generator. The images are generally obtained in the standing/sitting position and the posteroanterior direction. The obtained sequential images are utilized for clinical applications such as assessment of diaphragmatic motion, ventilation, and perfusion.
DXR = Dynamic X-ray

Computerized image processing techniques can facilitate the interpretation of hundreds of sequential images obtained by DXR and visualization of the results of subsequent dynamic analysis. These techniques include image registration for correction of physical motion (43, 44), bone suppression (45-50), automatic recognition of the lung area (51, 52), and motion tracking (53-56). In addition, some of the software and techniques previously developed for conventional chest radiography, digital fluoroscopy, and digital subtraction angiography (2, 57, 58) can also be utilized for DXR assessments. For example, the bone suppression software developed for conventional chest radiography can be used for DXR. Bone suppression is useful in image preprocessing because the ribs always overlay the lung field and affect the pixel value. In addition, the ribs often show different movement patterns from the lung, which interferes with dynamic motion analysis. It should be noted that a visual review of the original sequential images may be important because unpredictable events such as cough and body movement can sometimes interfere with the analysis.

Evaluation of Diaphragmatic Motion

The diaphragm is the most important respiratory muscle, and its kinetics are important for understanding physiological respiratory conditions. Diaphragmatic dysfunction is known to be caused by various diseases (Table 2) (59, 60). Lung

Table 1. An Example of Imaging Protocol

Tube voltage	100 kVp
Filter	0.5 mm Al + 0.1 mm Cu
Tube current	20–50 mA
Tube current-time	0.08–0.16 mAs/frame
Frame rate	7.5 or 15 or 30 frame/sec
Grid	80 line/cm
Pixel size	194 or 388 μm
Matrix size	1536 x 2048 or 768 x 1024 pixel
Source to image distance	2 m
Entrance surface dose	0.3–1.0 mGy for a 15 sec exam

https://doi.org/10.3348/kjr.2020.1136

Korean Journal of Radiology
KJR

disease is listed as one of the causes, and abnormal diaphragmatic motion has been reported in patients with COPD (61, 62).

For the analysis of diaphragmatic motion on DXR sequential images, the lung area is automatically determined using edge-detection methods (e.g., Prewitt Filter) (35). The highest point of each diaphragm is automatically tracked by the template-matching technique throughout the respiratory phase. Then, the vertical excursion and the peak motion speed of each diaphragm are calculated (Fig. 3).

In a clinical study, the movement of the diaphragm during the respiratory cycle in six healthy volunteers and a patient with emphysema was investigated with dynamic FPD imaging with computer analysis (24). The distance from the lung apex to the diaphragm was measured automatically, and this method was shown to be feasible as an index of the respiratory phase. The obtained respiratory phase information was utilized for further analysis of pulmonary ventilation. Eighteen participants (10 normal individuals and 8 patients) were further analyzed, and this method quantitatively showed continuous elevation of the left diaphragm during the whole respiratory cycle in two patients (25). In addition, excursions of the diaphragm in patients with interstitial pneumonia (n = 3) showed smaller values than the average value in normal subjects. These results suggest that DXR can be used for quantitative and functional evaluation of the diaphragm in conventional chest radiography.

The diaphragm motion during tidal breathing was investigated in 172 volunteers (35) and 39 COPD patients than in 47 normal subjects (36). DXR demonstrated that the motion of the left diaphragm was significantly larger and faster than that of the right diaphragm in volunteers. The average excursion of the left diaphragm was 14.9 ± 4.6 mm and that of the right diaphragm was 11.0 ± 4.0 mm (p < 0.001). In addition, a higher body mass index (BMI) and higher tidal volume showed a statistically significant

Table 2. Causes of Diaphragmatic Dysfunction

Location of the Lesion	Disease
Cerebral cortex	Vascular accident
Internal capsule	Vascular accident
	Arnold-Chiari disease
Central nervous system	Multiple sclerosis
Spinal cord	Traumatic degenerative (severe spondylosis)
Motor neurons	Post-polio syndrome
	Amyotrophic lateral sclerosis
	Syringomyelia
	Paraneoplastic neuropathy associated with antibodies
	Radiation post-irradiation
	Spinal muscular atrophy
Brachial plexus	Traumatic
	Iatrogenic (anaesthetic blockages, obstetric procedures, chiropractic manipulations of the neck, radiotherapy)
	Idiopathic
Phrenic	Trauma
	Compression/infiltration (mediastinal neoplasms)
	Guillain–Barré syndrome
	Infection (Herpes–Zoster virus, pneumonias, Lyme disease, Human immunodeficiency virus)
	Amyotrophic neuralgia (Parsonage-Turner syndrome)
	Thoracic surgeries
	Others (malnutrition, diabetes, hypothyroidism, benign thyroid hypertrophy, porphyria, vasculitis, Charcot-Marie-Tooth disease)
	Idiopathic
Lung	Chronic obstructive pulmonary disease, asthma
Neuromuscular junction	Myasthenia gravis, botulism, Lambert–Eaton syndrome
Muscular	Muscular dystrophies, steroid myopathy, Pompe disease, myositis, mechanical ventilation

Adapted from Ricoy et al. Pulmonology 2019;25:223-235 (60).

https://doi.org/10.3348/kjr.2020.1136

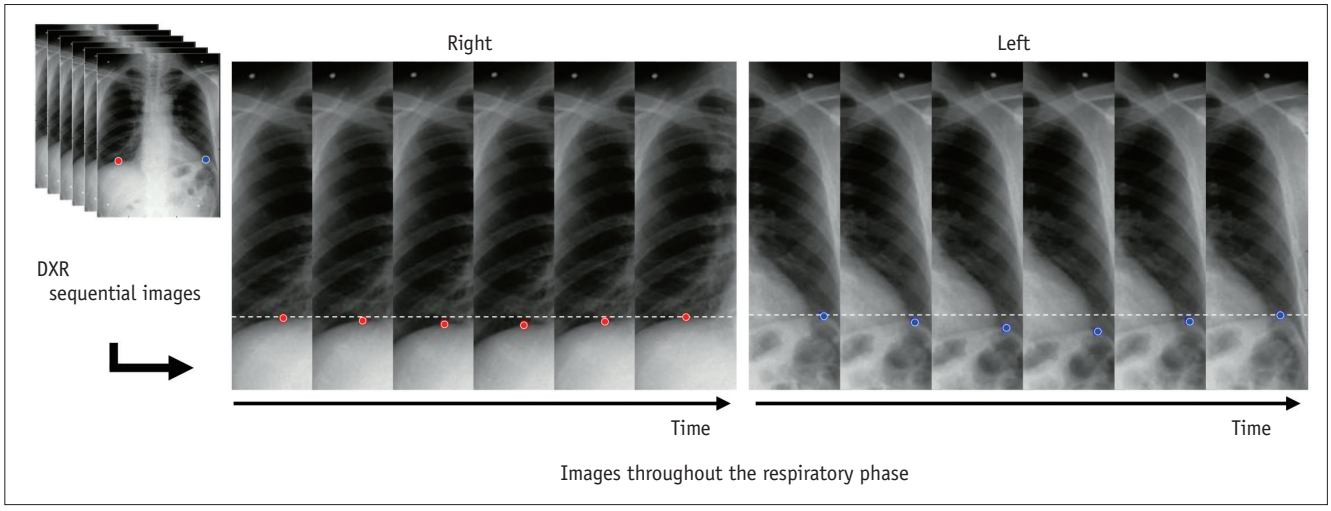

A

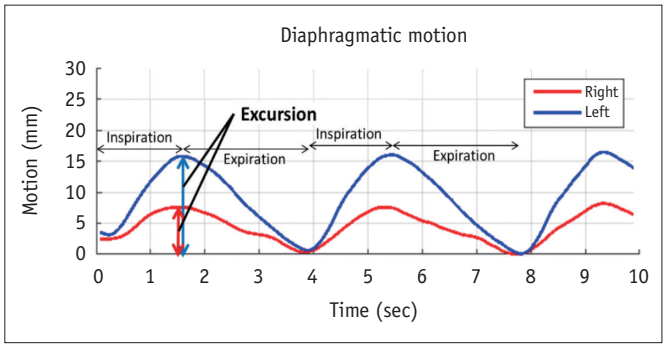

B

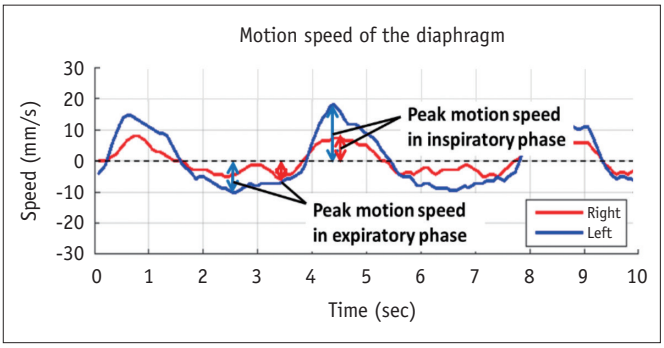

C

Fig. 3. Diaphragmatic motion analysis using DXR.
The highest point of each diaphragm (red and blue points) is automatically tracked by the template-matching technique throughout the respiratory phase **(A)**. The vertical excursions of the diaphragm on both sides are shown in a graph **(B)**. The peak motion speed of each diaphragm during inspiration and expiration can be calculated from inter-frame differences **(C)**.

association with increased excursions of the diaphragm ($p < 0.05$ for both BMI and tidal volume). In comparison with normal individuals, COPD patients showed a larger excursion of the diaphragm and faster peak motion in the inspiratory phase (right, 14.7 ± 5.5 mm vs. 10.2 ± 3.7 mm, $p < 0.001$; left, 17.2 ± 4.9 mm vs. 14.9 ± 4.2 mm, $p = 0.022$). COPD and higher BMI were independently associated with increased excursions ($p < 0.05$ for both COPD and BMI). The larger diaphragmatic excursion may be compensation for the abnormal gas exchange in COPD patients, and the greater diaphragmatic motion during tidal breathing can result in respiratory fatigue in daily life. The mechanism of the relationship between BMI and diaphragmatic motion is unclear, but increased oxygen consumption due to high BMI may influence the diaphragmatic motion (63).

The diaphragmatic motion during forced breathing was evaluated in 174 volunteers in one study (38) and 31 COPD patients and 31 normal individuals in another study (37). In the 174 normal volunteers, the motion of the left diaphragm was significantly larger and faster than that of the right during forced breathing as well as during tidal breathing. The average excursion of the left diaphragm was 52.1 ± 15.9 mm and that of the right was 49.1 ± 17.0 mm ($p < 0.001$). Higher BMI and vital capacity (VC) were associated with greater excursion and faster peak motion. In the second study, COPD patients were categorized into their respective Global Initiative for Chronic Obstructive Lung Disease (GOLD) groups. Patients with GOLD classifications 3 or 4 showed significantly decreased excursion in comparison with normal subjects (right, 39.8 ± 15.3 mm vs. 52.7 ± 15.1 mm, $p = 0.030$; left, 43.7 ± 14.0 mm vs. 56.9 ± 15.5 mm, $p = 0.017$) and patients with GOLD classifications 1 or 2 (right, 39.8 ± 15.3 mm vs. 54.4 ± 16.7 mm, $p = 0.036$; left, 43.7 ± 14.0 mm vs. 60.5 ± 13.9 mm, $p = 0.008$). The peak motion speed of the left diaphragm in the inspiratory phase in COPD patients was lower than that in normal individuals. The

https://doi.org/10.3348/kjr.2020.1136

Korean Journal of Radiology
KJR

excursions of the diaphragms showed correlations with VC, percent VC (%VC), and the ratio of forced expiratory volume in one second (FEV1). These results demonstrated that diaphragmatic motion tended to be more restricted in COPD patients than in normal individuals during forced breathing, contrary to tidal breathing.

Clinical examples of tidal breathing are shown in Figure 4 and Supplementary Movie 1–3. The cyclic motion of both

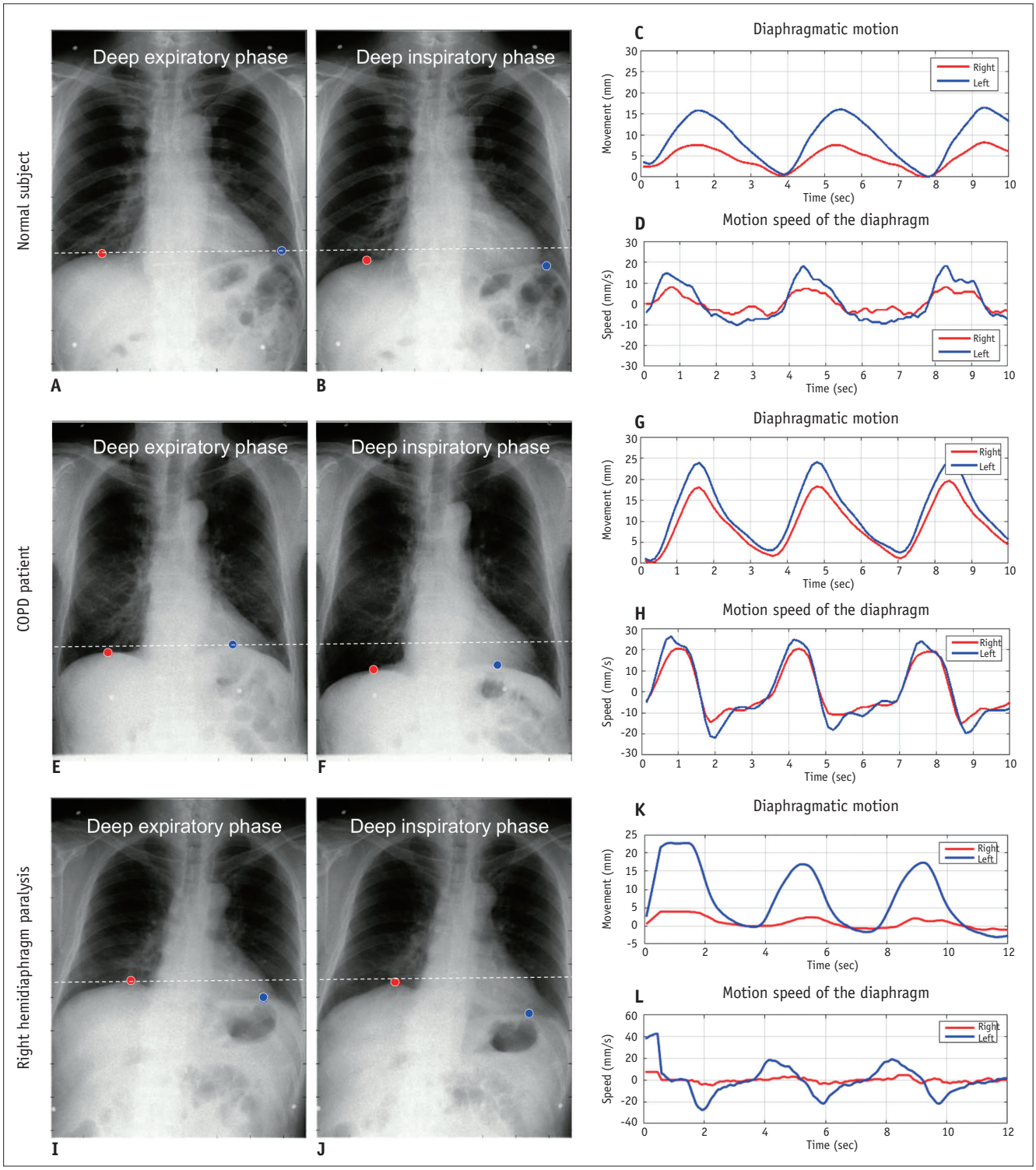

Fig. 4. Examples of diaphragmatic motion in tidal breathing.
A-D. A 60-year-old normal male. **E-H.** A 79-year-old male with COPD. **I-L.** A 76-year-old male with right hemidiaphragm paralysis. COPD = chronic obstructive pulmonary disease

https://doi.org/10.3348/kjr.2020.1136

diaphragms can be observed in a normal participant. In comparison with the normal participant, the COPD patient showed a larger excursion of the diaphragm and faster peak motion in the inspiratory phase. In the patient with right hemidiaphragm paralysis, the left diaphragm moved well during tidal breathing, whereas the right diaphragm moved little. Thus, diaphragmatic motion imaging using DXR has the potential to differentiate between normal individuals and patients with pulmonary diseases, including those with COPD, phrenic nerve palsy, post-cardiac surgery patients, or transplant recipients.

Ventilation Imaging

The translucency of the lung on chest radiography is influenced by various factors. It is increased by emphysema, lung cysts, bullae, and pneumothorax, and decreased by pulmonary lesions such as inflammation, edema, and fibrosis. In addition, it also changes dynamically during the respiratory and cardiac cycles (2, 24). During the inspiratory phase, the air volume inside the alveoli and/or bronchiole/bronchi increases, which results in a decrease in the pixel value on the radiograph (increased translucency). In contrast, during the expiratory phase, the air volume decreases, which results in an increase in the pixel value on the radiograph (decreased translucency). Pulmonary ventilation imaging on DXR can visualize these slight but dynamic changes in translucency during respiration.

For the analysis of pixel values in ventilation imaging, non-rigid image registration is useful to match the corresponding anatomic points on sequential images. The lung area is then determined and divided into small blocks (e.g., 5 x 5 pixels: 1.94 mm x 1.94 mm). The average pixel value of each small block is calculated in order to reduce the noise and artifacts caused by misregistration. Smoothing of pixel values in the time-axis direction is also useful for reducing the noise caused by the heartbeat and artifacts resulting from rib movement (25).

The determination of the respiratory phase is necessary for further evaluation. One method is to use the diaphragmatic kinetics curve (previous section: evaluation of diaphragmatic motion). The frames for the lowest and highest peaks of the kinetics curve were determined as the maximum inspiratory and expiratory frames, respectively (Fig. 3). For the tidal breathing image sets, the phases can be estimated by applying a low-pass filter to the pixel values in the time-axis direction (Fig. 5) (36). Generally,

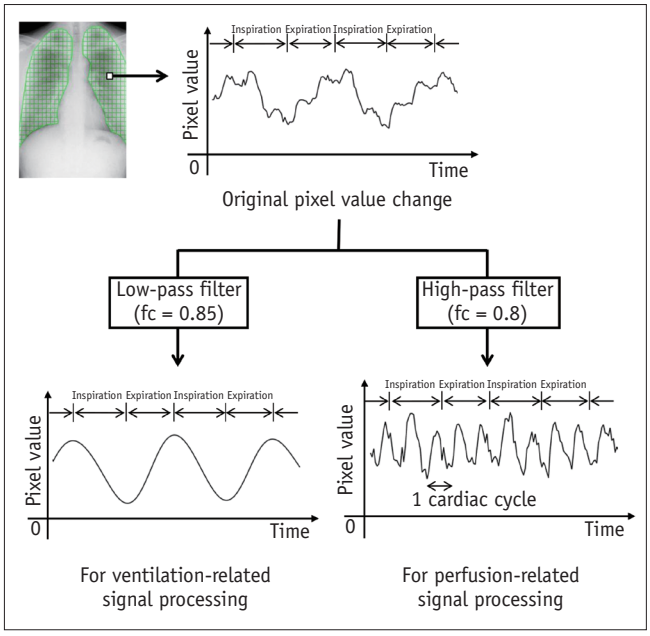

Fig. 5. Determination of the respiratory/cardiac phase. A low-pass filter (e.g., Parks-McClellan algorithm, fc = 0.85 Hz) extracts the low-frequency components (changes derived from ventilation) and eliminates the high-frequency components (changes derived from perfusion/blood flow). On the other hand, a high-pass filter (fc = 0.8) can extract the high-frequency components and eliminate the low-frequency components.

the frequency of breathing in adults is 12–20 cycles per minute, while the heart rate is 60–90 beats per minute. A low-pass filter (e.g., Parks-McClellan algorithm, fc = 0.85 Hz) extracts the low-frequency components (changes derived from ventilation) and eliminates the high-frequency components (changes derived from perfusion/blood flow). The respiratory phase can be determined directly from the time curve of the pixel value in each area after applying the filter.

To analyze ventilation, several types of signal processing are performed (Fig. 6). Inter-frame differences in the pixel value (pixel value change rate [PCR]) are assumed to represent pulmonary airflow at each time point in each local area (2). The maximum pixel value change rate (MPCR) during the inspiratory or expiratory phase is obtained by extracting the maximum pixel value change in each phase. MPCR is assumed to represent the maximum inspiratory or expiratory airflow in each local area. The difference in pixel values between the maximum inspiration and expiration frames reflects the extent of ventilation. The distribution of these functional values was visualized in fusion images with color maps. Other types of functional maps can be created using specific images depending on the diagnostic purpose.

One example of PCR maps involving a patient after

https://doi.org/10.3348/kjr.2020.1136

Korean Journal of Radiology
KJR

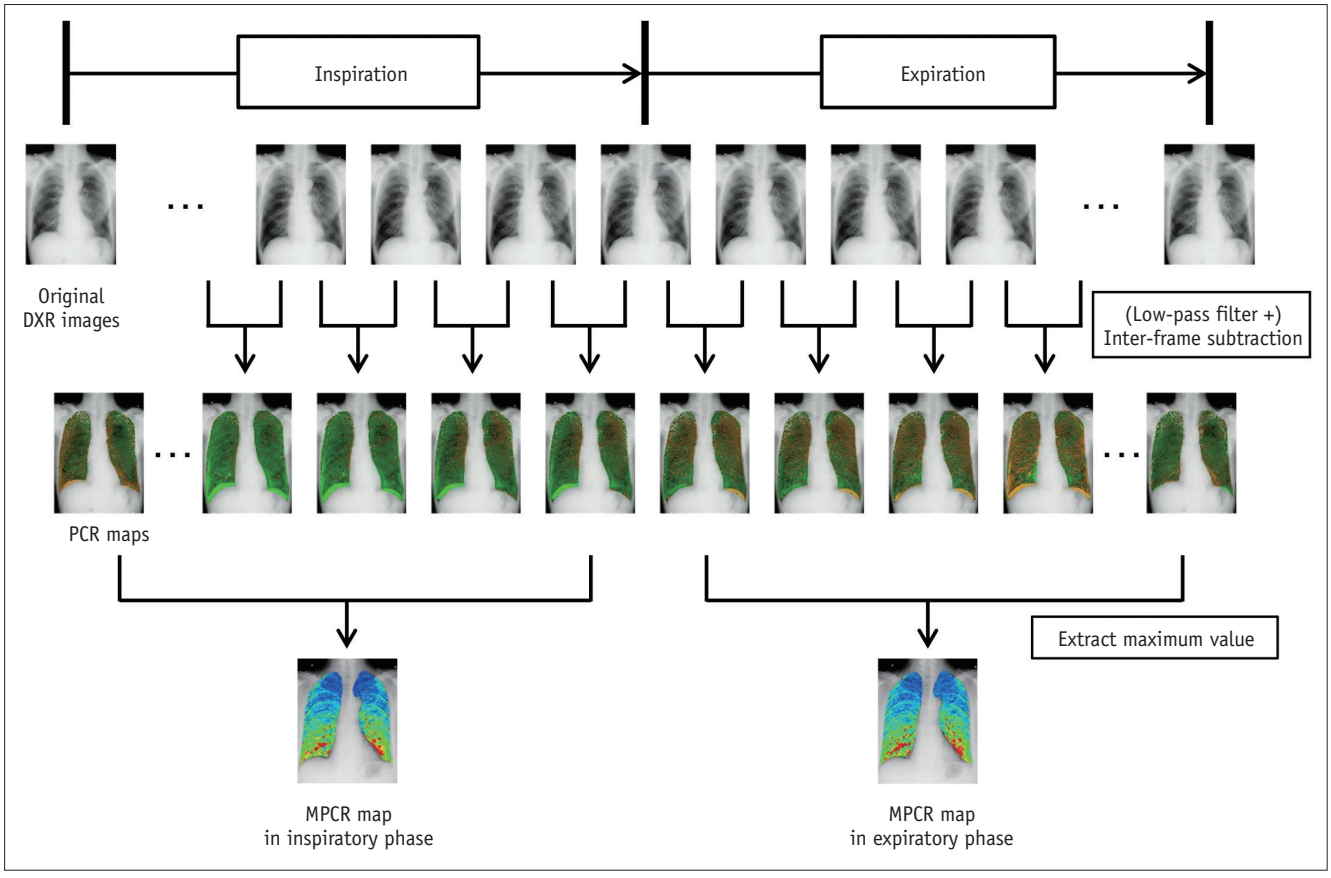

Fig. 6. Signal processing in ventilation analysis. PCR maps are obtained by calculation of the inter-frame difference in the pixel value (inter-frame subtraction). PCR is assumed to demonstrate pulmonary airflow at each time point. MPCR maps during the inspiratory or expiratory phases are obtained by extracting the maximum value in each phase. MPCR is assumed to represent the maximum airflow in each phase (see also Fig. 8). MPCR = maximum pixel value change rate, PCR = pixel value change rate

operation and radiation therapy is shown in Figure 7 and Supplementary Movie 4. The PCR (i.e., airflow) in the entire left lung seemed to be physiologically normal. The right middle lung area showed a pattern similar to that of the left lung, which suggests that the airflow in the area was preserved. On the other hand, the pixel value change in the right upper area was limited and some parts of the right area showed an inverse pattern compared with the left lung, which indicates that normal ventilation was impaired in these areas. It was difficult to analyze these findings only by conventional radiography. The CT image showed the preserved lung in the right middle area and a large cystic lesion in the right upper area. In the ventilation scintigraphy, weak ventilation could be observed in the right middle area, and ventilation in the right upper and lower areas was not preserved. These CT and scintigraphy findings support the results of the PCR map derived from DXR.

In an animal study, ventilation in a porcine model of atelectasis was evaluated using four pigs (32). A high linearity was reported between the pixel value change and tidal volume in the normal models ($r = 0.99$), and the pixel value change was significantly reduced in the areas of atelectasis ($p < 0.05$).

In a clinical study, six healthy volunteers were analyzed using these methods and the pixel value changes depending on the respiratory cycle were visualized; the pixel value tended to decrease in the inspiratory phase and increase in the expiratory phase (24). The difference between the maximum and minimum pixel values during the respiratory cycle was also evaluated, which reflects the difference in air volume between the inspiratory and expiratory phases (i.e., ventilation) in the local area. The difference in the upper lung field was less than that in the lower lung field, similar to the tendency observed for the regional differences in ventilation physiology.

Several patients with pulmonary diseases (n = 8) underwent further comparative investigations with CT images (25). The patients with emphysema and asthma

https://doi.org/10.3348/kjr.2020.1136

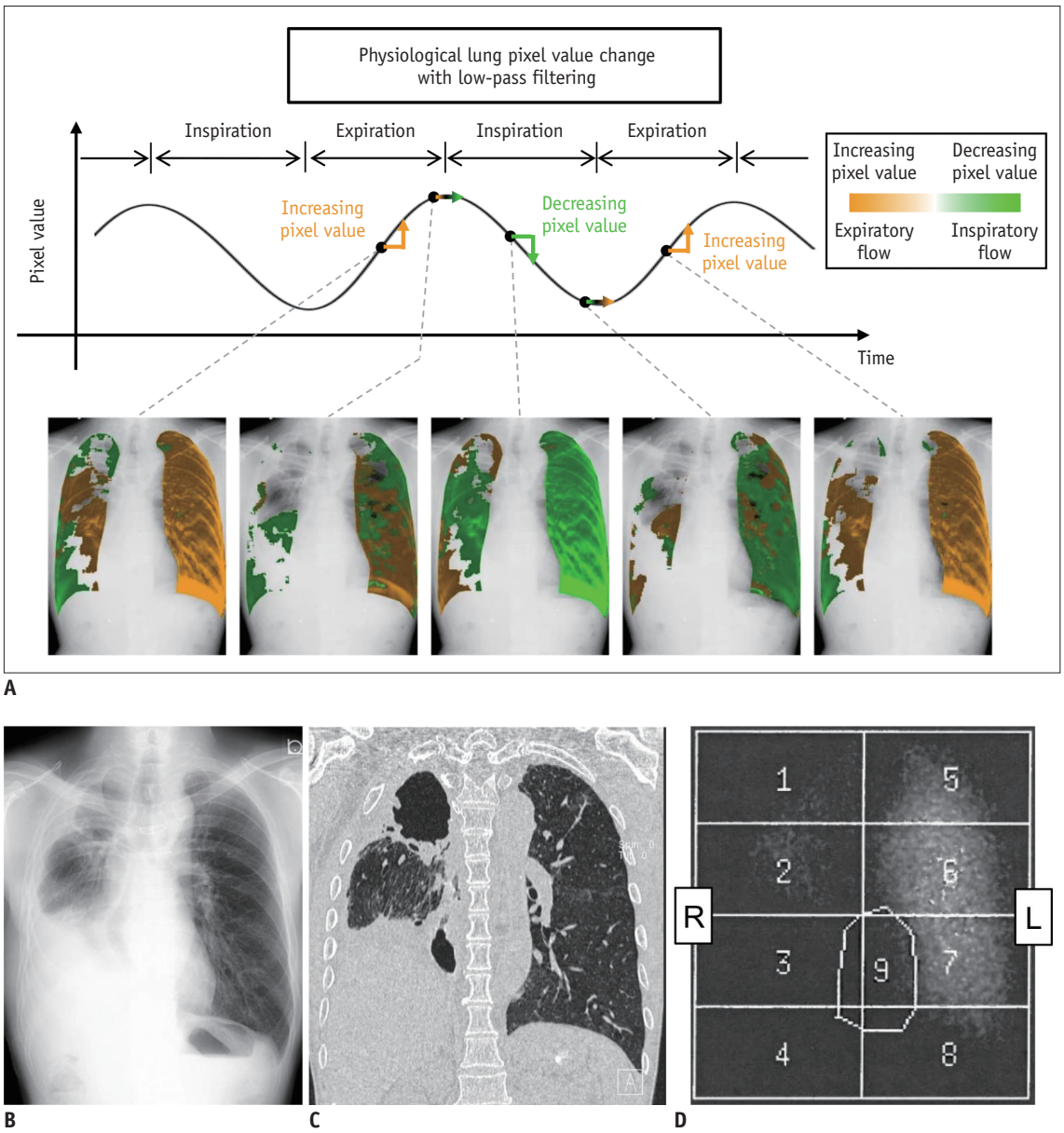

Fig. 7. A 68-year-old male after operation and radiotherapy for the right lung cancer.
A. PCR maps derived from DXR. In these images, an orange overlay indicates an increasing pixel value (i.e., expiratory flow) and a green overlay indicates a decreasing pixel value (i.e., inspiratory flow). **B.** Conventional radiography. **C.** CT image in the coronal view. **D.** Ventilation scintigraphy (anterior image).

showed lung areas with decreased inter-frame pixel value change (i.e., pulmonary airflow), and the area corresponded to the areas with air trapping or the emphysema lesion on CT images.

Twenty clinical cases (abnormal, n = 14; normal, n = 6) underwent assessments for the right-left symmetry in the distribution of respiratory-induced changes in pixel values on DXR in comparison with lung scintigraphy (30). The normal individuals showed a symmetrical distribution, whereas the participants with abnormalities showed an unsymmetrical distribution consistent with the abnormality. The distribution map visualized in the fusion image demonstrated reduced ventilation as well as that observed on lung scintigraphy.

The rate of change in the lung area from maximum inspiration to maximum expiration was assessed by DXR in 118 patients (lung cancer before surgery, n = 72; COPD, n = 35; asthma, n = 6; and asthma-COPD overlap syndrome, n = 5) (34). The rate was significantly associated with the ratio of the residual volume to total lung capacity (r = 0.48,

https://doi.org/10.3348/kjr.2020.1136

Korean Journal of Radiology
KJR

$p < 0.01$) and the percentage of predicted FEV1 (%FEV1; $r = -0.33$, $p < 0.01$). These findings suggested that the evaluation of the rate of change in the lung area using DXR may reflect air trapping.

Tidal ventilation was assessed in 43 patients with COPD and 47 normal individuals (36). DXR visualized the MPCR (i.e., maximum airflow) during the inspiratory or expiratory phase (Fig. 8). In normal individuals, MPCR in the lower lung field was larger than that in the upper lung field, and the MPCR showed a substantial craniocaudal gradient (Fig. 9). This finding indicates a larger airflow in the lower lung area. This is reasonable because the lower lungs physiologically show greater volume changes during breathing than the upper lungs because of the effects of gravity on lung recoil. On the other hand, in COPD patients (especially in severe COPD patients), the craniocaudal gradient of MPCR decreased. Thus, airflow obstruction in COPD may more strongly affect the airways of the lower lung field than those of the upper lung field. There was a moderate linear correlation between %FEV1 (representing the severity of COPD) and the quantified craniocaudal gradient ($r = 0.50$). Thus, DXR was able to detect kinetic and physiological respiratory changes and had the potential to allow evaluation of the severity of COPD.

Perfusion and V/Q Mismatch Imaging

Perfusion imaging on DXR visualizes the dynamic changes in X-ray translucency during the cardiac cycle. The pulmonary blood volume is approximately 500 mL and the

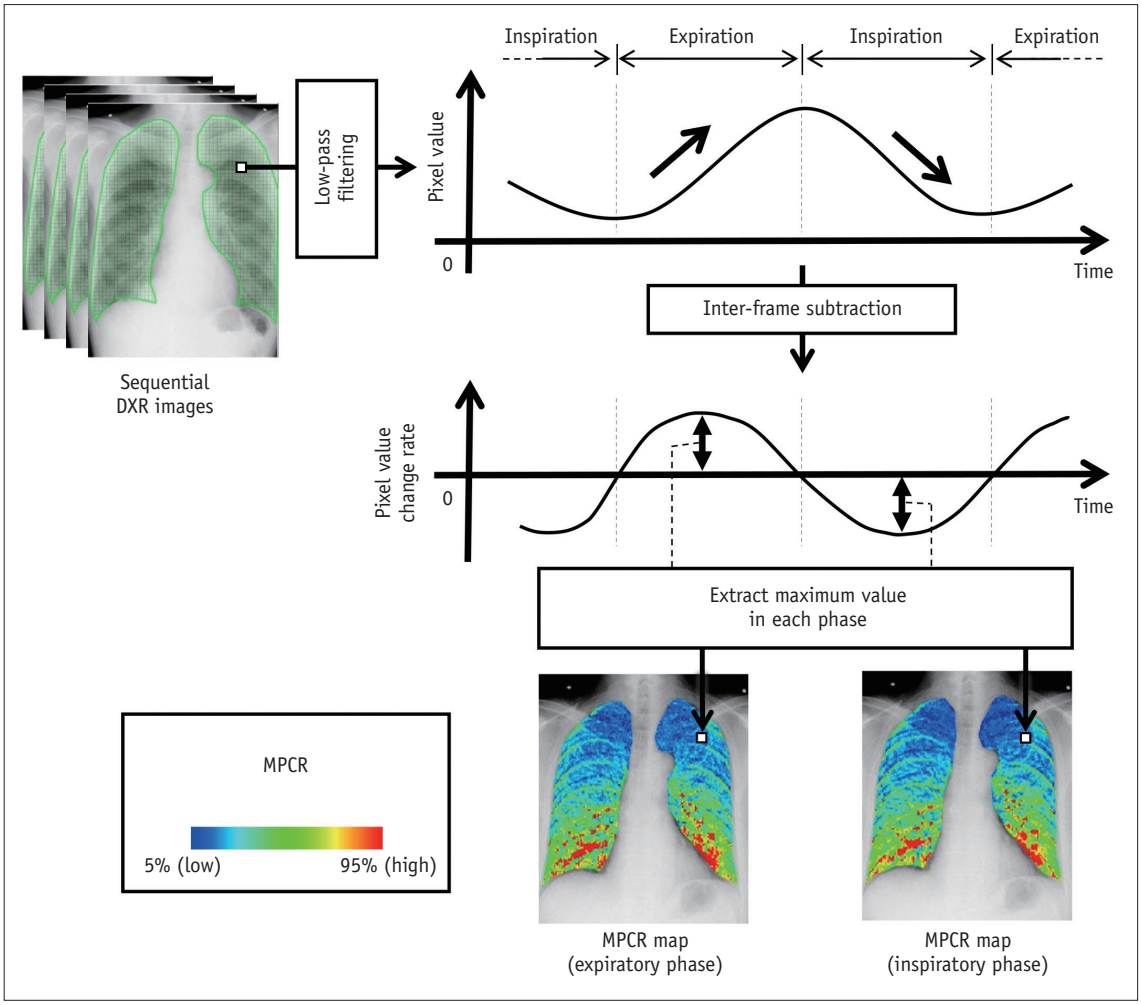

Fig. 8. Analysis of the MPCR. The lung area is divided into small blocks. Low-pass filtering is applied to the time curve of the pixel value in the block to extract the changes derived from ventilation. The PCR is calculated by inter-frame subtraction, which represents the pulmonary airflow at each time point in the block. The MPCR during the expiratory/inspiratory phase is obtained from the time curve of the PCR. MPCR represents the maximum airflow during the expiratory/inspiratory phase. Using the MPCR value in each block, the MPCR map is created for the expiratory/inspiratory phase. In the presented MPCR map, blue pixels indicate lower MPCR (less maximum airflow) and red pixels indicate higher MPCR (larger maximum airflow).

https://doi.org/10.3348/kjr.2020.1136

average pulmonary blood volume variation is 50–75 mL during a cardiac cycle (64, 65). The pixel value changes linearly with the blood volume in the lungs (41).

In perfusion imaging, image preprocessing steps such as image registration, division of the image into small blocks, and smoothing are useful as well as in ventilation imaging. The cardiac phase can be estimated by the motion rhythm of the ventricular wall using a motion tracking technique (2). The breath-holding images were used for this analysis and the rest expiratory level with breath-holding was appropriate because it is the most stable respiratory phase for patients. Instead of this method, the cardiac phase can be estimated by applying a high-pass filter (fc = 0.8) to non-breath-holding images (Fig. 5) (1). A high-pass filter can extract high-frequency components representing changes in pixel values related to perfusion/blood flow and eliminate the low-frequency components derived from ventilation.

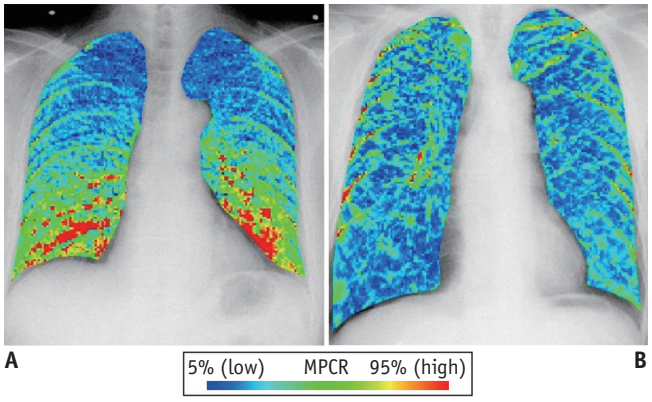

Fig. 9. MPCR maps in the expiratory phase in (A) a 60-year-old normal subject and (B) a 79-year-old COPD patient. Adapted from Yamada et al. Eur J Radiol 2017;92:37-44, with permission of authors (36).

Several methods can be used to obtain perfusion maps (1, 2). An example of signal processing using the signal curve correlation is shown in Figure 10 (1). Alternatively, functional maps are created by image subtraction between two specific images. The map of the change rate in the pixel value (i.e., flow velocity) can be estimated from inter-frame differences (2). The perfusion distribution map can be analyzed by subtracting the minimum intensity projection (MinIP) image in one cardiac cycle (representing pixel values with the least blood during the cycle) and the image at the early diastolic phase. The obtained distribution map represents the maximum differences in pixel values (i.e., relative perfusion). Other types of functional maps can be created using specific images depending on the purpose. In addition, ventilation-perfusion (V/Q) mismatch can be evaluated by combining ventilation and perfusion imaging using DXR (2, 66-68). V/Q mismatch is an important diagnostic factor for treatment strategy, and scintigraphy is generally used in the clinical setting (69, 70).

Examples are shown in Figure 11, Supplementary Movie 5, and Figure 12. Figure 11 and Supplementary Movie 5 present the findings for a patient with right pulmonary embolism (PE). The PCR map for ventilation suggested that

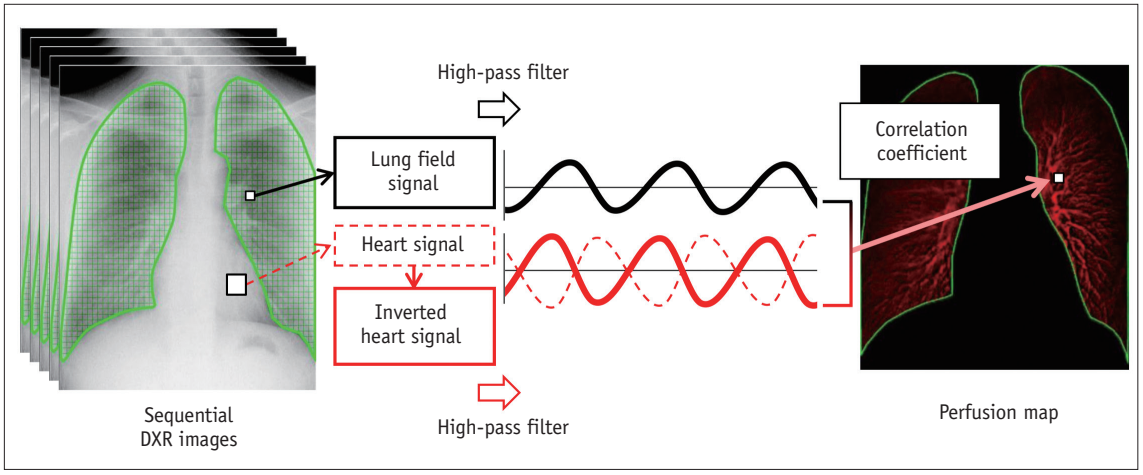

Fig. 10. Prototype signal processing for perfusion imaging. Locate the ROI in the lung field and heart area and apply a high-pass filter to both signal curves to extract the cardiac cycle signal. Obtain an inverted heart signal that is assumed to reflect the pattern of the pulmonary artery flow. Calculate the correlation coefficient between the lung signal curve and inverted heart signal curve. A large coefficient indicates good consistency between the lung field signal and pulmonary artery flow pattern and preserved perfusion. A perfusion map is obtained as a color map of the spatial distribution of the correlation coefficient. Repeat the calculation of the correlation coefficient by shifting the inverted heart signal curve in the time axis, because it is assumed that pulmonary artery flow timing varies depending on the location in the lung field. Finally, the obtained perfusion maps are output as a movie.

https://doi.org/10.3348/kjr.2020.1136

Korean Journal of Radiology
KJR

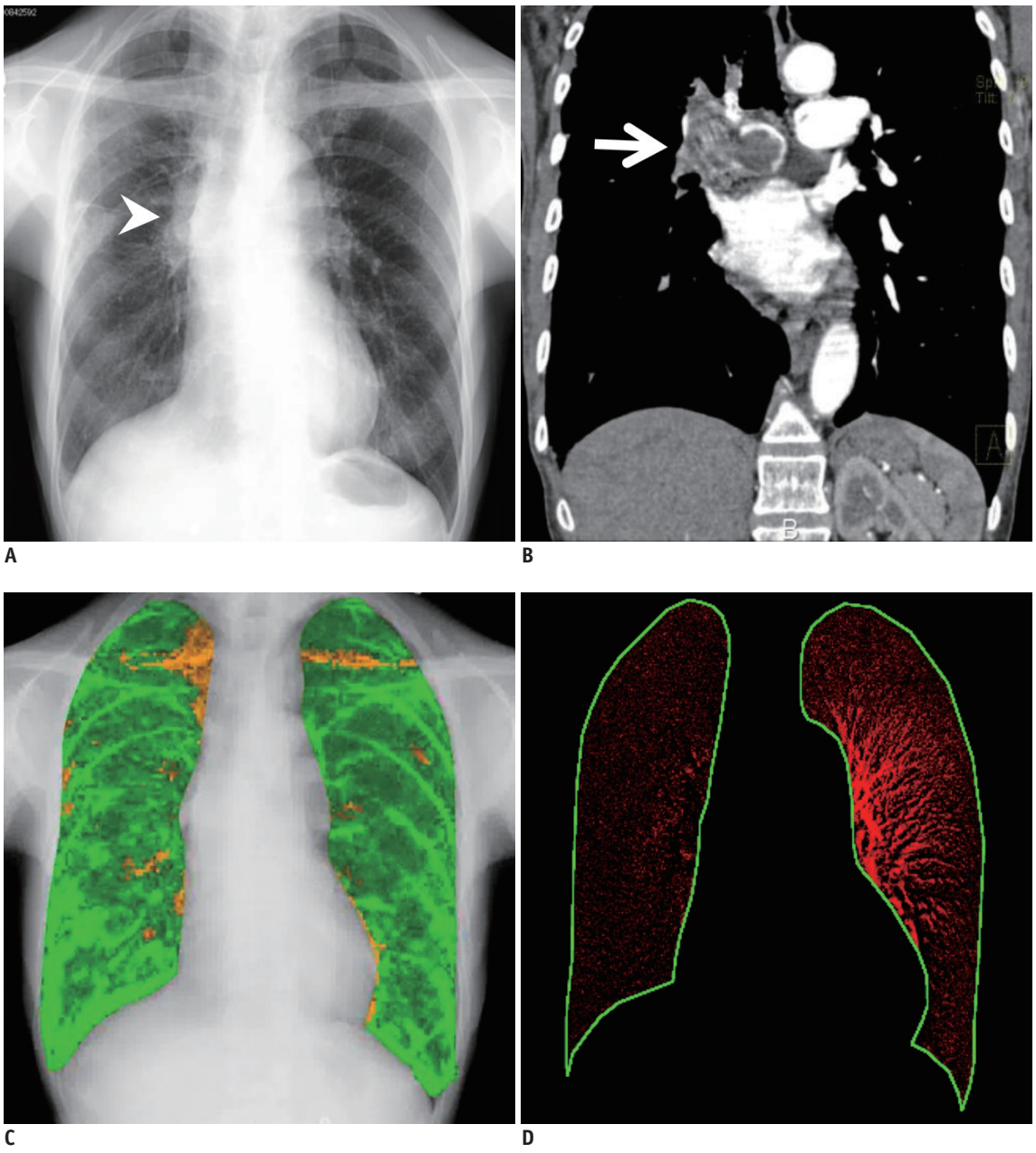

Fig. 11. A 75-year-old female with massive right pulmonary embolism.
A. Conventional radiograph. **B.** Coronal contrast-enhanced CT image. **C.** PCR map for ventilation obtained using DXR in the inspiratory phase. **D.** Perfusion map obtained using DXR. The conventional radiograph showed a slight enlargement of the right hilum (arrowhead). Massive right pulmonary embolism is seen in the contrast-enhanced CT image (arrow). The PCR map indicated that the airflow was preserved in almost the whole area of both lungs. However, in the perfusion map, the signal in the right lung was decreased in comparison with that in the left lung.

both lungs had normal airflow. However, the perfusion map obtained using DXR showed decreased perfusion in the right lung in comparison with that in the left lung. Thus, a V/Q mismatch was suggested using DXR. Figure 12 shows a patient with right pulmonary artery thromboembolism. In this patient, DXR suggested a decrease in the perfusion signal in the middle and lower areas of the right lung, which was consistent with scintigraphy.

In an animal study, perfusion in a porcine PE model was evaluated using six pigs (31). The lobes affected by PE showed a mean reduction of 49.6% in pixel values in comparison with the unaffected lobes within the same subject, and a mean reduction of 41.3% in comparison with that before blockage in the same lobe. In all PE models, the perfusion distribution map using DXR was consistent with the perfusion defects confirmed in the corresponding

https://doi.org/10.3348/kjr.2020.1136

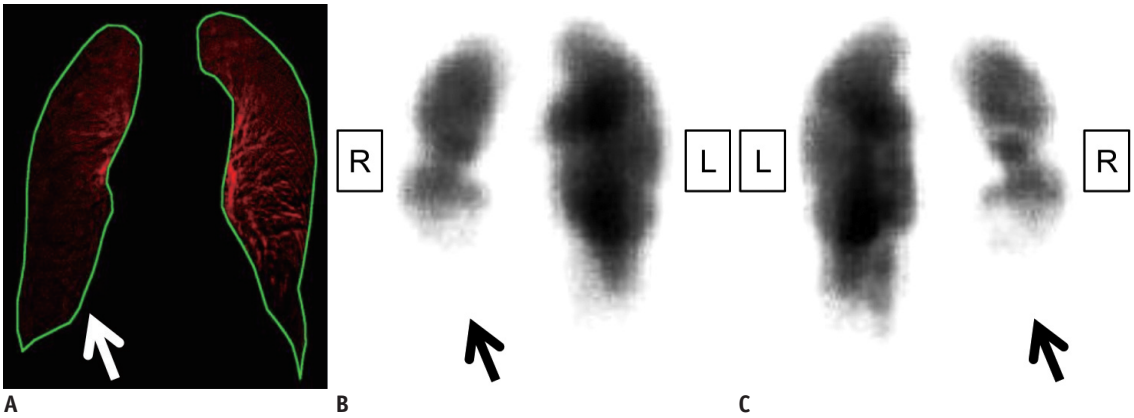

Fig. 12. A 35-year-old female with right pulmonary artery thromboembolism.
A. A perfusion map derived from DXR. Anterior **(B)** and posterior views of perfusion scintigraphy (99mTc-MAA) **(C)**. The perfusion signal in the middle and lower areas of the right lung was decreased in the perfusion map derived from DXR (white arrow), which was consistent with the findings obtained with scintigraphy (black arrows). 99mTc-MAA = technetium 99mTc macro aggregated albumin

contrast-enhanced images.

In a clinical study, 20 participants (normal, n = 8; abnormal, n = 12, including patients with COPD, asthma, bronchiolitis obliterans, atelectasis, and interstitial pulmonary fibrosis) were assessed using DXR perfusion imaging, and lung perfusion scintigraphy (technetium 99mTc macro aggregated albumin [99mTc-MAA]) (27). In the normal participants, DXR visualized the normal pulmonary blood flow distribution, which decreased gradually and symmetrically from the hilar region to the peripheral regions. In most patients with pulmonary diseases such as pulmonary fibrosis, the distribution of the pixel value change in DXR was consistent with scintigraphy findings. Notably, in two cases, the results obtained using DXR perfusion imaging were different from those obtained with scintigraphy; DXR showed a false-positive area (the perfusion was reduced in the DXR, but not in scintigraphy). The imaging principles are different between scintigraphy and DXR perfusion imaging; 99mTc-MAA is trapped in the capillary, and scintigraphy reflects the distribution of the pulmonary artery blood flow. On the other hand, DXR uses X-ray translucency and reflects blood volume changes (27). In addition, the body position during imaging is also different; scintigraphy is performed in a supine position, but DXR is usually performed in a standing position. DXR may not properly visualize the lung field behind the heart and diaphragm. These differences might result in discrepancies between the two modalities.

In a case report involving a patient with a V/Q mismatch (hypoxemia, 74-year-old male), both ventilation and perfusion imaging using DXR showed a significant correlation with the radioisotope counts in scintigraphy (ventilation: $r = 0.78$, perfusion: $r = 0.77$) (66). The V/Q ratio using DXR also showed a significant correlation with that calculated from scintigraphy results ($r = 0.78$).

Challenges and Future Perspectives of DXR

As mentioned above, DXR offers many advantages: sequential images with a high temporal resolution during the whole respiration and/or cardiac cycle, large FOV entirely covering both lungs, low radiation dose, which is much lower than that of CT, flexibility in the body position, lack of dependence on radioactive materials or contrast media, the ability to apply previously developed techniques for X-ray imaging, and accessibility, including cost-effectiveness, small space, and high throughput. However, DXR is also associated with several challenges.

Three-dimensional anatomical information cannot be obtained using DXR. To address this issue, lateral-view DXR may be useful. Although the lateral view does not include complete 3-dimensional information, it can reveal motion of the diaphragm, chest wall, and lung behind the diaphragm on the PA view. Thus, a combination of PA and lateral views can provide a deeper understanding of respiratory physiology.

Quantification is not perfect in DXR-based ventilation/perfusion analysis. The absolute value of ventilation or perfusion cannot be calculated from DXR analysis because DXR mainly utilizes the relative change in X-ray translucency. Contrast media containing iodine and xenon gas may help quantify perfusion and ventilation (71-73).

https://doi.org/10.3348/kjr.2020.1136

Korean Journal of Radiology
KJR

However, accessibility is one of the biggest advantages of DXR, and it is important to adopt a simple procedure without contrast media. With DXR, simple assessments for screening or follow-up may be more suitable than detailed evaluations, which require quantitative analysis. Screening and follow-up assessments are good candidates for utilizing DXR in clinical situations because of its advantages such as cost-effectiveness, high throughput, and low radiation dose.

There are still relatively few reports regarding the clinical usefulness of DXR. More evidence for this technique is necessary to facilitate its wider use in clinical situations. Further clinical studies to investigate its ability to diagnose various diseases and predict clinical outcomes will lead to establishment of diagnostic criteria for DXR. Comparisons with other modalities, including scintigraphy, will also be useful for understanding the characteristics of DXR. There may be some differences between scintigraphy and DXR because they differ in imaging mechanisms and procedures. These studies will clarify how DXR and scintigraphy should be used properly, depending on the purpose.

Further technical developments will contribute to improvements in DXR. Computer-aided diagnosis (CAD) schemes are essential for interpretation of DXR findings because DXR includes information that is difficult to interpret only by visual evaluation. Analyses of the chest wall, such as rib kinematics, may add further diagnostic value to DXR (58). Sophisticated color maps or other ways to make the abnormality recognizable at a glance using CAD will facilitate clinical evaluations by radiologists and clinicians (74). Moreover, the recently emerged deep learning techniques have enabled the development of a wide variety of algorithms. Many studies have focused on using chest radiography with deep-learning-based algorithms to achieve high accuracy comparable to that obtained with human experts (75-79). We can utilize not only those previously developed algorithms but also newer deep learning techniques to develop appropriate algorithms to analyze DXR. Furthermore, hardware techniques such as dual-energy methods may be used to improve the usefulness of DXR. One animal study reported that bone suppression using a dynamic dual-energy radiography system was feasible for lung ventilation analysis and motion tracking of lung anatomic features (50). Updates in both software and hardware will improve the performance of DXR.

The studies on diaphragmatic motion introduced in this article focused on only the highest points of the diaphragms. However, assessment of the motion of the entire diaphragm is possible. In addition, the motion of the chest wall and lung field can be observed using non-rigid image registration on DXR images. Moreover, these applications may be useful for dynamic evaluation of the spine, joints, muscles, bones, or heart and great vessels, and may not be limited to the lungs and diaphragms. These assessments may provide further diagnostic value.

As mentioned in the sections above, assessments using DXR showed a correlation with the results of pulmonary function tests (PFTs). Moreover, the projected lung areas on DXR have been shown to be correlated with PFT results (80). The recent pandemic of coronavirus disease 2019 (COVID-19) requires contact inhibition, and PFTs are unsuitable for assessments under these conditions. DXR has the potential to serve as an alternative to PFTs in patients with suspected or confirmed COVID-19 or other infectious diseases. It may also facilitate the assessment of suspected COVID-19 patients in the future, particularly in areas where access to CT scanners is limited. Patients with COVID-19 pneumonia may continue to experience dyspnea for a long time. Some investigators have reported the development of fibrotic lung disease in these patients (81, 82). As the COVID-19 pandemic continues, evaluation of pulmonary function in COVID-19 patients will be important in the future.

Knowledge of anatomy and physiology and clinical practice can help leverage the information in DXR. This would require close collaboration among radiologists, clinicians, researchers in physiology, technologists, software developers, and machine vendors to overcome the challenges and achieve advances in DXR.

CONCLUSION

DXR is a functional imaging technique that uses sequential images obtained by FPD and provides useful information for the evaluation of diaphragmatic motion, ventilation, and lung perfusion. Computerized image processing techniques are utilized to process the obtained images and to visualize the outcomes. In comparison with other functional imaging modalities, DXR shows advantages such as a high temporal resolution, flexibility in the subject position, and accessibility. DXR may also serve as an alternative method for PFTs in subjects requiring contact prohibition, thereby facilitating the assessment of COVID-19 patients in the future. We would like to emphasize that it is important to further develop the DXR perfusion method,

 https://doi.org/10.3348/kjr.2020.1136

which can evaluate pulmonary perfusion without contrast media, large amounts of nuclear medicine agents, or a high levels of radiation exposure. Further clinical studies are required to establish DXR as a valuable diagnostic tool before generalized clinical utilization of this new technology becomes possible.

Supplementary Materials

The Data Supplement is available with this article at https://doi.org/10.3348/kjr.2020.1136.

Supplementary Movie Legends

Movie 1. Diaphragmatic motion during tidal breathing in a 60-year-old normal male. The red and blue points represent the highest points of each diaphragm.

Movie 2. Diaphragmatic motion during tidal breathing in a 79-year-old male with COPD. The red and blue points represent the highest points of each diaphragm.

Movie 3. Diaphragmatic motion during tidal breathing in a 76-year-old male with right hemidiaphragm paralysis. The red and blue points represent the highest points of each diaphragm.

Movie 4. PCR maps in a 68-year-old male after surgery and radiotherapy for right lung cancer.

Movie 5. Perfusion maps in a 75-year-old female with massive right pulmonary embolism.

Conflicts of Interest

Reserch funding from Canon Inc., Canon Medical Systems Inc., and Konica-Minolta Inc.; Consultant to Canon Medical Systems Inc., and Mitsubishi Chemical Co. for outside of the submitted work. Other authors have no conflict of interest.

ORCID iDs

Akinori Hata
https://orcid.org/0000-0003-1149-7094
Yoshitake Yamada
https://orcid.org/0000-0002-5842-5349

REFERENCES

1. Yamada Y, Ueyama M, Abe T, Araki T, Nishino M, Jinzaki M, et al. Dynamic chest radiography using flat panel detector system: technique and applications. Dps2016.rsna.org Web site. https://dps2016.rsna.org/exhibit/?exhibit=CH112-ED-X. Published November 2016. Accessed November 11, 2020
2. Tanaka R. Dynamic chest radiography: flat-panel detector (FPD) based functional X-ray imaging. *Radiol Phys Technol* 2016;9:139-153
3. Mortensen J, Berg RMG. Lung scintigraphy in COPD. *Semin Nucl Med* 2019;49:16-21
4. Win T, Laroche CM, Groves AM, White C, Wells FC, Ritchie AJ, et al. Use of quantitative lung scintigraphy to predict postoperative pulmonary function in lung cancer patients undergoing lobectomy. *Ann Thorac Surg* 2004;78:1215-1218
5. Kim NH, Delcroix M, Jais X, Madani MM, Matsubara H, Mayer E, et al. Chronic thromboembolic pulmonary hypertension. *Eur Respir J* 2019;53:1801915
6. Johns CS, Swift AJ, Rajaram S, Hughes PJC, Capener DJ, Kiely DG, et al. Lung perfusion: MRI vs. SPECT for screening in suspected chronic thromboembolic pulmonary hypertension. *J Magn Reson Imaging* 2017;46:1693-1697
7. Ter-Karapetyan A, Triphan SMF, Jobst BJ, Anjorin AF, Ley-Zaporozhan J, Ley S, et al. Towards quantitative perfusion MRI of the lung in COPD: the problem of short-term repeatability. *PLoS One* 2018;13:e0208587
8. Weidman EK, Plodkowski AJ, Halpenny DF, Hayes SA, Perez-Johnston R, Zheng J, et al. Dual-energy CT angiography for detection of pulmonary emboli: incremental benefit of iodine maps. *Radiology* 2018;289:546-553
9. Masy M, Giordano J, Petyt G, Hossein-Foucher C, Duhamel A, Kyheng M, et al. Dual-energy CT (DECT) lung perfusion in pulmonary hypertension: concordance rate with V/Q scintigraphy in diagnosing chronic thromboembolic pulmonary hypertension (CTEPH). *Eur Radiol* 2018;28:5100-5110
10. Zhang G, Dilling TJ, Stevens CW, Forster KM. Functional lung imaging in thoracic cancer radiotherapy. *Cancer Control* 2008;15:112-119
11. Doganay O, Matin T, Chen M, Kim M, McIntyre A, McGowan DR, et al. Time-series hyperpolarized xenon-129 MRI of lobar lung ventilation of COPD in comparison to V/Q-SPECT/CT and CT. *Eur Radiol* 2019;29:4058-4067
12. Yamasaki Y, Abe K, Hosokawa K, Kamitani T. A novel pulmonary circulation imaging using dynamic digital radiography for chronic thromboembolic pulmonary hypertension. *Eur Heart J* 2020;41:2506
13. Verschakelen JA, Deschepper K, Jiang TX, Demedts M. Diaphragmatic displacement measured by fluoroscopy and derived by Respitrace. *J Appl Physiol (1985)* 1989;67:694-698
14. Kleinman BS, Frey K, VanDrunen M, Sheikh T, DiPinto D, Mason R, et al. Motion of the diaphragm in patients with chronic obstructive pulmonary disease while spontaneously breathing versus during positive pressure breathing after anesthesia and neuromuscular blockade. *Anesthesiology* 2002;97:298-305
15. Fujita H, Doi K, MacMahon H, Kume Y, Giger ML, Hoffmann KR, et al. Basic imaging properties of a large image intensifier-TV digital chest radiographic system. *Invest Radiol* 1987;22:328-335

16. Desprechins B, Luypaert R, Delrée M, Freson M, Malfroot A, Dab I, et al. Evaluation of time interval difference digital subtraction fluoroscopy in patients with cystic fibrosis. *Scand J Gastroenterol Suppl* 1988;143:86-92
17. Lam KL, Chan HP, MacMahon H, Oravecz WT, Doi K. Dynamic digital subtraction evaluation of regional pulmonary ventilation with nonradioactive xenon. *Invest Radiol* 1990;25:728-735
18. Hoffmann KR, Doi K, Fencil LE. Determination of instantaneous and average blood flow rates from digital angiograms of vessel phantoms using distance-density curves. *Invest Radiol* 1991;26:207-212
19. Kiuru A, Svedström E, Kuuluvainen I. Dynamic imaging of pulmonary ventilation. Description of a novel digital fluoroscopic system. *Acta Radiol* 1991;32:114-119
20. Kiuru A, Svedström E, Korvenranta H, Kuuluvainen I. Dynamic pulmonary imaging: performance properties of a digital fluoroscopy system. *Med Phys* 1992;19:467-473
21. Srinivas Y, Wilson DL. Image quality evaluation of flat panel and image intensifier digital magnification in x-ray fluoroscopy. *Med Phys* 2002;29:1611-1621
22. Vano E, Geiger B, Schreiner A, Back C, Beissel J. Dynamic flat panel detector versus image intensifier in cardiac imaging: dose and image quality. *Phys Med Biol* 2005;50:5731-5742
23. Yamada Y, Ueyama M, Abe T, Araki T, Abe T, Nishino M, et al. Difference in diaphragmatic motion during tidal breathing in a standing position between COPD patients and normal subjects: time-resolved quantitative evaluation using dynamic chest radiography with flat panel detector system ("dynamic X-ray phrenicography"). *Eur J Radiol* 2017;87:76-82
24. Tanaka R, Sanada S, Suzuki M, Kobayashi T, Matsui T, Inoue H, et al. Breathing chest radiography using a dynamic flat-panel detector combined with computer analysis. *Med Phys* 2004;3:2254-2262
25. Tanaka R, Sanada S, Okazaki N, Kobayashi T, Fujimura M, Yasui M, et al. Evaluation of pulmonary function using breathing chest radiography with a dynamic flat panel detector: primary results in pulmonary diseases. *Invest Radiol* 2006;41:735-745
26. Tanaka R, Sanada S, Okazaki N, Kobayashi T, Suzuki M, Matsui T, et al. Detectability of regional lung ventilation with flat-panel detector-based dynamic radiography. *J Digit Imaging* 2008;21:109-120
27. Tanaka R, Sanada S, Fujimura M, Yasui M, Tsuji S, Hayashi N, et al. Pulmonary blood flow evaluation using a dynamic flat-panel detector: feasibility study with pulmonary diseases. *Int J Comput Assist Radiol Surg* 2009;4:449-455
28. Tanaka R, Samei E, Segars P, Abadi E, Roth H, Oda H, et al. *Dynamic chest radiography for pulmonary function diagnosis: a validation study using 4D extended cardiac-torso (XCAT) phantom*. Proceedings of SPIE 10948, Medical Imaging 2019: Physics of Medical Imaging, 109483I-1-8; 2019 Feb 17-20; San Diego, CA, USA: Medical Imaging
29. Hiasa Y, Otake Y, Tanaka R, Sanada S, Sato Y. Recovery of 3D rib motion from dynamic chest radiography and CT data using local contrast normalization and articular motion model. *Med Image Anal* 2019;51:144-156
30. Tanaka R, Sanada S, Fujimura M, Yasui M, Tsuji S, Hayashi N, et al. Ventilatory impairment detection based on distribution of respiratory-induced changes in pixel values in dynamic chest radiography: a feasibility study. *Int J Comput Assist Radiol Surg* 2011;6:103-110
31. Tanaka R, Tani T, Nitta N, Tabata T, Matsutani N, Muraoka S, et al. Detection of pulmonary embolism based on reduced changes in radiographic lung density during cardiac beating using dynamic flat-panel detector: an animal-based study. *Acad Radiol* 2019;26:1301-1308
32. Tanaka R, Tani T, Nitta N, Tabata T, Matsutani N, Muraoka S, et al. Pulmonary function diagnosis based on respiratory changes in lung density with dynamic flat-panel detector imaging: an animal-based study. *Invest Radiol* 2018;53:417-423
33. Tamura M, Matsumoto I, Saito D, Yoshida S, Takata M, Tanaka R, et al. Dynamic chest radiography: novel and less-invasive imaging approach for preoperative assessments of pleural invasion and adhesion. *Radiol Case Rep* 2020;15:702-704
34. Ohkura N, Kasahara K, Watanabe S, Hara J, Abo M, Sone T, et al. Dynamic-ventilatory digital radiography in air flow limitation: a change in lung area reflects air trapping. *Respiration* 2020;99:382-388
35. Yamada Y, Ueyama M, Abe T, Araki T, Abe T, Nishino M, et al. Time-resolved quantitative analysis of the diaphragms during tidal breathing in a standing position using dynamic chest radiography with a flat panel detector system ("dynamic X-ray phrenicography"): initial experience in 172 volunteers. *Acad Radiol* 2017;24:393-400
36. Yamada Y, Ueyama M, Abe T, Araki T, Abe T, Nishino M, et al. Difference in the craniocaudal gradient of the maximum pixel value change rate between chronic obstructive pulmonary disease patients and normal subjects using sub-mGy dynamic chest radiography with a flat panel detector system. *Eur J Radiol* 2017;92:37-44
37. Hida T, Yamada Y, Ueyama M, Araki T, Nishino M, Kurosaki A, et al. Decreased and slower diaphragmatic motion during forced breathing in severe COPD patients: time-resolved quantitative analysis using dynamic chest radiography with a flat panel detector system. *Eur J Radiol* 2019;112:28-36
38. Hida T, Yamada Y, Ueyama M, Araki T, Nishino M, Kurosaki A, et al. Time-resolved quantitative evaluation of diaphragmatic motion during forced breathing in a health screening cohort in a standing position: dynamic chest phrenicography. *Eur J Radiol* 2019;113:59-65
39. Körner M, Weber CH, Wirth S, Pfeifer KJ, Reiser MF, Treitl M. Advances in digital radiography: physical principles and system overview. *Radiographics* 2007;27:675-686
40. Kawashima H, Tanaka R, Matsubara K, Ichikawa K, Sakuta K, Minami S, et al. *Temporal-spatial characteristic evaluation in a dynamic flat-panel detector system*. Proceedings of SPIE 7622, Medical Imaging 2010: Physics of Medical Imaging, 76224T-1-

 https://doi.org/10.3348/kjr.2020.1136

8; 2019 Feb 17-20; San Diego, CA, USA: Medical Imaging
41. Tanaka R, Sanada S, Tsujioka K, Matsui T, Takata T, Matsui O. Development of a cardiac evaluation method using a dynamic flat-panel detector (FPD) system: a feasibility study using a cardiac motion phantom. *Radiol Phys Technol* 2008;1:27-32
42. International Atomic Energy Agency. International basic safety standards for protection against ionizing radiation and for the safety of radiation sources. Gnssn.iaea.org Web site. https://gnssn.iaea.org/Superseded%20Safety%20Standards/Safety_Series_115_1996_Pub996_EN.pdf. Published 1996. Accessed November 11, 2020
43. Kano A, Doi K, MacMahon H, Hassell DD, Giger ML. Digital image subtraction of temporally sequential chest images for detection of interval change. *Med Phys* 1994;21:453-461
44. Ishida T, Ashizawa K, Engelmann R, Katsuragawa S, MacMahon H, Doi K. Application of temporal subtraction for detection of interval changes on chest radiographs: improvement of subtraction images using automated initial image matching. *J Digit Imaging* 1999;12:77-86
45. Suzuki K, Abe H, MacMahon H, Doi K. Image-processing technique for suppressing ribs in chest radiographs by means of massive training artificial neural network (MTANN). *IEEE Trans Med Imaging* 2006;25:406-416
46. Oda S, Awai K, Suzuki K, Yanaga Y, Funama Y, MacMahon H, et al. Performance of radiologists in detection of small pulmonary nodules on chest radiographs: effect of rib suppression with a massive-training artificial neural network. *AJR Am J Roentgenol* 2009;193:W397-W402
47. Freedman MT, Lo SC, Seibel JC, Bromley CM. Lung nodules: improved detection with software that suppresses the rib and clavicle on chest radiographs. *Radiology* 2011;260:265-273
48. Schalekamp S, van Ginneken B, Meiss L, Peters-Bax L, Quekel LG, Snoeren MM, et al. Bone suppressed images improve radiologists' detection performance for pulmonary nodules in chest radiographs. *Eur J Radiol* 2013;82:2399-2405
49. Miyoshi T, Yoshida J, Aramaki N, Matsumura Y, Aokage K, Hishida T, et al. Effectiveness of bone suppression imaging in the detection of lung nodules on chest radiographs: relevance to anatomic location and observer's experience. *J Thorac Imaging* 2017;32:398-405
50. Xu T, Ducote JL, Wong JT, Molloi S. Dynamic dual-energy chest radiography: a potential tool for lung tissue motion monitoring and kinetic study. *Phys Med Biol* 2011;56:1191-1205
51. Xu XW, Doi K. Image feature analysis for computer-aided diagnosis: accurate determination of ribcage boundary in chest radiographs. *Med Phys* 1995;22:617-626
52. Candemir S, Antani S. A review on lung boundary detection in chest X-rays. *Int J Comput Assist Radiol Surg* 2019;14:563-576
53. Hoffmann KR, Doi K, Chen SH, Chan HP. Automated tracking and computer reproduction of vessels in DSA images. *Invest Radiol* 1990;25:1069-1075
54. Shirato H, Shimizu S, Kunieda T, Kitamura K, van Herk M, Kagei K, et al. Physical aspects of a real-time tumor-tracking system for gated radiotherapy. *Int J Radiat Oncol Biol Phys* 2000;48:1187-1195
55. Chen QS, Weinhous MS, Deibel FC, Ciezki JP, Macklis RM. Fluoroscopic study of tumor motion due to breathing: facilitating precise radiation therapy for lung cancer patients. *Med Phys* 2001;28:1850-1856
56. Terunuma T, Tokui A, Sakae T. Novel real-time tumor-contouring method using deep learning to prevent mistracking in X-ray fluoroscopy. *Radiol Phys Technol* 2018;11:43-53
57. Tanaka R, Sanada S, Sakuta K, Kawashima H. Improved accuracy of markerless motion tracking on bone suppression images: preliminary study for image-guided radiation therapy (IGRT). *Phys Med Biol* 2015;60:N209-N218
58. Tanaka R, Sanada S, Sakuta K, Kawashima H. Quantitative analysis of rib kinematics based on dynamic chest bone images: preliminary results. *J Med Imaging (Bellingham)* 2015;2:024002
59. Nason LK, Walker CM, McNeeley MF, Burivong W, Fligner CL, Godwin JD. Imaging of the diaphragm: anatomy and function. *Radiographics* 2012;32:E51-70
60. Ricoy J, Rodríguez-Núñez N, Álvarez-Dobaño JM, Toubes ME, Riveiro V, Valdés L. Diaphragmatic dysfunction. *Pulmonology* 2019;25:223-235
61. Suga K, Tsukuda T, Awaya H, Takano K, Koike S, Matsunaga N, et al. Impaired respiratory mechanics in pulmonary emphysema: evaluation with dynamic breathing MRI. *J Magn Reson Imaging* 1999;10:510-520
62. Unal O, Arslan H, Uzun K, Ozbay B, Sakarya ME. Evaluation of diaphragmatic movement with MR fluoroscopy in chronic obstructive pulmonary disease. *Clin Imaging* 2000;24:347-350
63. Womack CJ, Hyman BA, Gardner AW. Prediction of peak oxygen consumption in patients with intermittent claudication. *Angiology* 1998;49:591-598
64. Davies A, Moores C. Structure of the respiratory system, related to function. *The Respiratory System* 2010:11-28
65. Ugander M, Jense E, Arheden H. Pulmonary intravascular blood volume changes through the cardiac cycle in healthy volunteers studied by cardiovascular magnetic resonance measurements of arterial and venous flow. *J Cardiovasc Magn Reson* 2009;11:42
66. Tanaka R, Sanada S, Fujimura M, Yasui M, Tsuji S, Hayashi N, et al. *Dynamic chest radiography with a flat-panel detector (FPD): ventilation-perfusion study*. Proceedings of SPIE 7965, Medical Imaging 2011: Biomedical Applications in Molecular, Structural, and Functional Imaging, 76224T-1-7; 2011 Feb 13-16; Lake Buena Vista, FL, USA: Medical Imaging
67. Tanaka R, Matsumoto I, Tamura M, Takata M, Kasahara K, Ohkura N, et al. Comparison of dynamic flat-panel detector-based chest radiography with nuclear medicine ventilation-perfusion imaging for the evaluation of pulmonary function: a clinical validation study. *Med Phys* 2020 Jul [Epub]. https://doi.org/10.1002/nbm.3665
68. Yamasaki Y, Hosokawa K, Tsutsui H, Ishigami K. Pulmonary ventilation-perfusion mismatch demonstrated by dynamic

chest radiography in giant cell arteritis. *Eur Heart J* 2020 Jun [Epub]. https://doi.org/10.1093/eurheartj/ehaa443
69. Petersson J, Glenny RW. Gas exchange and ventilation-perfusion relationships in the lung. *Eur Respir J* 2014;44:1023-1041
70. Thomas KS, Mann A, Williams J. Pulmonary (V/Q) imaging. *J Nucl Med Technol* 2018;46:87-88
71. Sakamoto A, Sakamoto I, Nagayama H, Koike H, Sueyoshi E, Uetani M. Quantification of lung perfusion blood volume with dual-energy CT: assessment of the severity of acute pulmonary thromboembolism. *AJR Am J Roentgenol* 2014;203:287-291
72. Park EA, Goo JM, Park SJ, Lee HJ, Lee CH, Park CM, et al. Chronic obstructive pulmonary disease: quantitative and visual ventilation pattern analysis at xenon ventilation CT performed by using a dual-energy technique. *Radiology* 2010;256:985-997
73. Kong X, Sheng HX, Lu GM, Meinel FG, Dyer KT, Schoepf UJ, et al. Xenon-enhanced dual-energy CT lung ventilation imaging: techniques and clinical applications. *AJR Am J Roentgenol* 2014;202:309-317
74. Pérez JS, Meinhardt-Llopis E, Facciolo G. TV-L1 optical flow estimation. *Image Processing On Line* 2013;3:137-150
75. Cicero M, Bilbily A, Colak E, Dowdell T, Gray B, Perampaladas K, et al. Training and validating a deep convolutional neural network for computer-aided detection and classification of abnormalities on frontal chest radiographs. *Invest Radiol* 2017;52:281-287
76. Lakhani P, Sundaram B. Deep learning at chest radiography: automated classification of pulmonary tuberculosis by using convolutional neural networks. *Radiology* 2017;284:574-582
77. Majkowska A, Mittal S, Steiner DF, Reicher JJ, McKinney SM, Duggan GE, et al. Chest radiograph interpretation with deep learning models: assessment with radiologist-adjudicated reference standards and population-adjusted evaluation. *Radiology* 2020;294:421-431
78. Nasr-Esfahani E, Samavi S, Karimi N, Soroushmehr SM, Ward K, Jafari MH, et al. Vessel extraction in X-ray angiograms using deep learning. *Annu Int Conf IEEE Eng Med Biol Soc* 2016:643-646
79. Yang S, Kweon J, Roh JH, Lee JH, Kang H, Park LJ, et al. Deep learning segmentation of major vessels in X-ray coronary angiography. *Sci Rep* 2019;9:16897
80. Hino T, Hata A, Hida T, Yamada Y, Ueyama M, Araki T, et al. Projected lung areas using dynamic X-ray (DXR). *Eur J Radiol Open* 2020;7:100263
81. George PM, Wells AU, Jenkins RG. Pulmonary fibrosis and COVID-19: the potential role for antifibrotic therapy. *Lancet Respir Med* 2020;8:807-815
82. Spagnolo P, Balestro E, Aliberti S, Cocconcelli E, Biondini D, Casa GD, et al. Pulmonary fibrosis secondary to COVID-19: a call to arms? *Lancet Respir Med* 2020;8:750-752